

Revision of two-temperature magnetically arrested flows onto a black hole

M. MOŚCIBRODZKA¹

¹*Department of Astrophysics/IMAPP, Radboud University, P.O. Box 9010, 6500 GL Nijmegen, The Netherlands*

ABSTRACT

We revisit radiative properties of 3-D GRMHD two-temperature magnetically arrested disk (MAD) models in which electrons are heated up by magnetic turbulent cascade. We focus on studying the models emission which characteristics include variability in both total intensity and linear/circular polarizations as well as rotation measures at energies around synchrotron emission peak in millimeter waves. We find that radiative properties of MAD models with turbulent electron heating are well converged with respect to the numerical grid resolution, which has not been demonstrated before. We compare radiation from the two-temperature simulations with turbulent heating to single-temperature models with electron temperatures calculated based on commonly used $R(\beta)$ prescription. We find that the two-temperature models do not significantly overperform the $R(\beta)$ models and in practice may be indistinguishable from the $R(\beta)$ models. Accounting for physical effects such as radiative cooling and non-thermal electron distribution function makes a weak impact on properties of millimeter emission. Models are scaled to Sgr A* - an accreting black hole in the center of our galaxy, and compared to the most complete observational datasets. We point out consistencies and inconsistencies between the MAD models and observations of this source and discuss future prospects for GRMHD simulations.

Keywords: Supermassive black holes (1663), Magnetohydrodynamical simulations (1966), Low-luminosity active galactic nuclei (2033), Plasma physics (2089)

1. INTRODUCTION

Magnetically arrested disks (hereafter MADs) is a class of solutions of black hole accretion initially developed for radiatively inefficient accretion flows (RIAF) (Igumenshchev et al. 2003; Narayan et al. 2003; Proga & Begelman 2003; Tchekhovskoy et al. 2011; McKinney et al. 2012; Narayan et al. 2022). In MADs realized in general relativistic magnetohydrodynamics (GRMHD) simulations, the magnetic field flux accumulated near the black hole event horizon is extreme, which has two important consequences. First, the power of jets produced in MAD simulations is significant, making the jet opening angle rather large (~ 55 deg, Chael et al. 2019). This is consistent with what is observed in sub-Eddington accreting black hole systems such as M87 (Walker et al. 2018; Kim et al. 2018). MADs near black hole horizon are further supported in M87 by the first polarimetric images from the Event Horizon Telescope

(EHT; Event Horizon Telescope Collaboration et al. 2021). Second, the jet magnetosphere in MADs is often reconnecting at the equatorial plane of the simulation causing magnetic field flux eruptions into the disk body. Such flux eruptions has been proposed to explain flaring behaviour of another sub-Eddington accreting supermassive black hole, Sgr A* (Dexter et al. 2020b; Porth et al. 2021; Wielgus et al. 2022b). It has been also recently found that horizon scale polarimetric images of Sgr A* are more consistent with MADs (Event Horizon Telescope Collaboration et al. 2024). While less magnetized standard and normal evolution accretion disks (SANEs) are not completely ruled out by observations of any of the sources, MAD RIAF solution become a leading candidate to explain observations of two best-resolved aforementioned accreting supermassive black holes.

One of the most uncertain parts of MADs (but also SANEs) is how they generate emission. In the aforementioned class of systems, where the accreting plasma is collisionless, electron and ion distribution functions remain unknown. Typically, to mimic the collisionless effects in models we assume that the plasma has two-

temperature structure and we “paint” electron temperatures on the top of the GRMHD models according to some parameterized law. One example of such parameterized law is the $R(\beta)$ prescription of Mościbrodzka et al. 2016 used in Event Horizon Telescope Collaboration et al. 2022, where model parameter $R(\beta) \equiv T_i/T_e(\beta)$ is a ratio of non-emitting ion to emitting electron temperatures that depends on the local plasma β ($\equiv P_{\text{mag}}/P_{\text{gas}}$) parameter. Other than the $R(\beta)$ models has been proposed (Mościbrodzka & Falcke 2013; Mościbrodzka et al. 2014; Chan et al. 2015; Gold et al. 2017; Anantua et al. 2020). Alternatively, one can assume a non-thermal electron distribution function, but those are typically also parametric (see e.g., Davelaar et al. 2018; Scepi et al. 2022; Cruz-Osorio et al. 2022; Fromm et al. 2022; Zhao et al. 2023 for a recent work and Chael et al. 2017; Petersen & Gammie 2020 for examples of models with evolution of non-thermal electrons). Finally one can model two-temperature GRMHD flows where electron temperatures are followed by a separate equation which includes non-adiabatic (viscous), sub-grid heating terms based on plasma or particle-in-cell considerations (Howes 2010; Rowan et al. 2017; Kawazura et al. 2019) and radiative cooling terms (e.g., Ryan et al. 2018).

The method to track electron temperatures in GRMHD simulations assuming a sub-grid model for ion and electron heating has been introduced by Ressler et al. (2015). Sadowski et al. (2017) further developed the idea to add the ion/electron pressure as well as self-consistent variable adiabatic index to the GRMHD evolution. Two-temperature 2-D and 3-D GRMHD models have been carried out in the past, specifically for Sgr A* (Ressler et al. 2017; Sadowski et al. 2017; Chael et al. 2018; Dexter et al. 2020a; Jiang et al. 2023) and M87 (Ryan et al. 2018; Mizuno et al. 2021; Dihingia et al. 2023).

In this paper we revisit the two-temperature GRMHD MAD simulations. The mentioned previous studies use several numerical codes assuming various: torus sizes, magnetic field topologies, adiabatic indices and grid resolutions to investigate the problem. It was not clear to us that the radiative output of these models is converged for MAD models with setups comparable to those in the EHT simulation library (Event Horizon Telescope Collaboration et al. 2022). The second motivation for the revision of two-temperature simulations is the fact that the MAD models with $R(\beta)$ prescription have typically too variable total intensity when compared to the observations of Sgr A* (Wielgus et al. 2022a; Event Horizon Telescope Collaboration et al. 2022). The origin of the discrepancy between the models and observations is un-

known. One possibility is that the $R(\beta)$ model, which was initially developed for the SANE simulations, is not appropriate for MADs and more sophisticated electron model should be adopted. One could also ask, how physically motivated is the $R(\beta)$ model for electron temperatures when considering MADs. The latter is relevant for all sub-Eddington accreting black hole systems. Finally, the measurement of black hole spin in EHT and other sources is typically accretion model dependent. A robust understanding of the dissipation processes in accreting plasma near the event horizon is critical for reliable spin estimates.

In this work, we investigate how numerical model parameters impact radiative (total intensity and polarimetric) characteristics of the two-temperature MAD simulations. We first demonstrate that they are independent of grid resolution used in GRMHD simulations. Next, we evolve models for longer times and compare the two-temperature models to $R(\beta)$ models. Finally, having checked that the results are weakly dependent on the exact shape of the electron distribution function and that they remain unchanged even when radiative cooling is introduced (scaling models to Sgr A* system), we compare the prograde and retrograde two-temperature MAD models to the newest multi-frequency polarimetric millimeter observational data of Sgr A*. In contrast to most of the previous two-temperature simulations, in our comparisons we focus on variability and polarization, which together are significantly more informative than the time-averaged or total intensity comparisons. We discuss the future prospects for investigating thermodynamics of the GRMHD simulations.

The paper is structured as follows. In Section 2 we describe our 3-D two-temperature GRMHD simulations setups and outline the details of radiative transfer modeling. In Section 3, we report the results and compare the models to selected observations of Sgr A*. We discuss the results and conclude in Section 4.

2. MODELS

2.1. GRMHD simulations

MAD simulations are carried by means of `ebhlight`, general relativistic radiation magnetohydrodynamics code developed and made public by Ryan et al. (2015). `ebhlight` is a relativistic, second-order, conservative, constrained-transport code for stationary spacetimes. While the fluid part of the code is based on `harm` routines (Gammie et al. 2003), the radiation part is based on `grmonty` scheme (Dolence et al. 2009).

All simulations are set in geometrized units where the lengthscale and timescale are set by the black hole mass: $\mathcal{L} \equiv GM/c^2$ and $\mathcal{T} \equiv GM/c^3$ (assuming $G = c = 1$ both

time and distances are measured in units of mass, M). The simulations start from the Fishbone-Moncrief torus (Fishbone & Moncrief 1976) at the equatorial plane of a Schwarzschild or Kerr black hole. The torus is described by two parameters: inner radius $r_{\text{in}} = 20M$ and radius of the pressure maximum, $r_{\text{max}} = 41M$. The torus is seeded with weak poloidal magnetic fields described by vector potential:

$$(A_r, A_\theta, A_\phi) = (0, 0, \frac{\rho}{\rho_{\text{max}}} \left(\frac{r}{r_{\text{in}}}\right)^3 \exp\left(\frac{r}{r_0}\right) \sin^3 \theta - 0.2) \quad (1)$$

where r, θ are the radius and polar angle in Kerr-Schild coordinates, parameter $r_0 = 400$, ρ is the plasma density. The initial magnetic field is renormalized so that initially plasma $\beta_{\text{max}} = 100$.

The simulations use ideal equation of state with constant adiabatic index of $\gamma_{\text{ad}} = 13/9$, i.e., we assume that plasma is a pure hydrogen with non-relativistic protons and relativistic electrons, for which adiabatic indices are $\gamma_p = 5/3$ and $\gamma_e = 4/3$, respectively.

All simulations are carried out in mixed modified Kerr-Schild logarithmic coordinates where resolution is focused on equatorial plane and towards the central region close to the black hole horizon. The grid stretches from within the black hole event horizon until $r_{\text{out}} = 1,000M$.

The grid refinement convergence test runs are integrated for 10,000M assuming four grid resolutions listed in Table 1. Convergence runs are done for black hole spin $a_* = 0$. Later in the paper we consider both prograde and retrograde fiducial models (also listed in Table 1) with the following spin values $a_* = -0.9375, -0.5, 0, 0.5, 0.9375$. Prograde and zero spin models are evolved until 30,000M, and retrograde models are evolved for a shorter times, only until 14,000M. Fiducial models have grid resolutions $(N_r, N_\theta, N_\phi) = (240, 120, 128)$ (for $a_* = -0.5, 0, 0.5$) and $(N_r, N_\theta, N_\phi) = (266, 120, 128)$ (for $a_* = -0.9375, 0.9375$). All models above are run with radiative modules of `ebhlight` turned off. We carry out one test run with radiative effects turned on. The parameters of the exploratory GRRMHD model are shown in Table 1.

2.2. Radiative transfer

We measure model convergence by studying their radiative properties. To predict synchrotron emission from the simulations, we post-process the GRMHD snapshots using ray-tracing relativistic polarized radiative transfer code `ipole` (Mościbrodzka & Gammie 2018). The radiative transfer calculations are typically carried out starting at later times of simulations when the accretion flow is relaxed from the initial conditions (starting

times, t_s , and final times, t_f , of all radiative transfer post-processing simulations are listed in Table 1). We scale all GRMHD simulations using mass and distance of Sgr A* black hole. Models density scale is set by \mathcal{M} , a standard mass (or accretion rate, \dot{M}) scaling factor, to produce average Sgr A* total flux of 2-3Jy observed at frequency of 229 GHz (Wielgus et al. 2022a). Table 1 lists each model \mathcal{M} and corresponding \dot{M} . Given the electron temperature model (see next sub-section), the imaging code produces synchrotron emission maps at a desired frequency ν (here 86–229 GHz) and a viewing angle i . Initially all maps are computed for a default viewing angle $i = 160$ deg selected based on recent re-discovery of a transient hot spot orbiting around Sgr A* (Wielgus et al. 2022b, see also viewing angle estimates by Yfantis et al. 2024) and then later for additional viewing angles $i = 150, 130, 110$ deg. Note that for the modeled source lower viewing angles are favored by EHT observations which revealed symmetric ring (Event Horizon Telescope Collaboration et al. 2022), hence we do not model emission for high viewing angles, $i \sim 90$ deg. Assuming $i > 90$ deg also guarantees the correct sign of the circular polarization for the assumed polarity of magnetic fields in the GRMHD models. Our model map resolution is 256×256 pixels and field-of-view = $120M \approx 600 \mu\text{as}$. A time-series of maps/images with cadence of $\Delta t = 10M$ is synthesized into light-curves in Stokes $\mathcal{I}, \mathcal{Q}, \mathcal{U}, \mathcal{V}$. Following Wielgus et al. 2022a modulation index $M_3 \equiv \sigma_{\Delta T} / \mu_{\Delta T}$ (ratio of standard deviation to mean flux calculated on time intervals $\Delta T = 3\text{h}$) is used to characterize light-curve variability in Stokes \mathcal{I} at two frequencies, 86 and 229 GHz. We also calculate spectral index in total intensity (α_I between 213–229 GHz), (Faraday) rotation measure (RM between 213–229 GHz), and linear (LP) and circular (CP) fractional polarizations at 86 and 229 GHz. These particular quantities are studied because they are later compared directly to observations. In our models Faraday rotation is caused by relativistic and sub-relativistic electrons within 100M from the event horizon; these electrons constitute so called internal Faraday screen.

2.3. Electron distribution functions

Following scheme of Ressler et al. (2015), the `ebhlight` code tracks total and electron entropies that are used to calculate the non-adiabatic (viscous) gas heating rates and evolve electron temperatures. The scheme requires providing a sub-grid model for proton-to-electron heating ratio, Q_p^+ / Q_e^+ . In this work we adopt prescription for Q_p^+ / Q_e^+ developed by Kawazura et al. (2019) (henceforth model K) which approximates dissi-

pation in a turbulent cascade with a functional form:

$$\frac{Q_p^+}{Q_e^+} = \frac{35}{1 + (\beta/15)^{-1.4} \exp^{-0.1T_e/T_p}}. \quad (2)$$

In this model most of the dissipation goes to protons in high β plasma regions, while electrons receive most of the heating in low β regions. Qualitatively, model K is very similar to turbulent heating model by [Howes \(2010\)](#). Other Q_p^+/Q_e^+ options are discussed in Section 4.

In ideal GRMHD models studied here using conservative code, the total viscous heating is produced by truncation errors at the numerical grid level. One may conclude that no matter what fraction of this heating goes to the electrons, this heating will be completely artificial. However, for the turbulent torus problem, the grid-scale dissipation is set by the large-scale turbulence in the problem (see section 3.1 in [Ressler et al. 2015](#) for more detailed discussion). The numerical scheme for electron heating implemented in `ebhlight` has been carefully tested against some analytic problems by [Ressler et al. \(2015\)](#) and [Ryan et al. \(2017\)](#) as well as [Sadowski et al. \(2017\)](#) who, except for the mentioned modifications, follows the same idea when evolving electron temperatures alone. We are not going to repeat these tests here. In `ebhlight` the electron evolution also does not include Coulomb couplings, unless radiative transfer is activated (see Section 3.2.1). Those are however not important in low density gas considered here. In `ebhlight` the electron temperature tracking is passive; i.e. the electron pressure is not accounted for in the GRMHD equations. More importantly, the proton (non-adiabatic/viscous) heating is not taken into account in the GRMHD equations as well; instead the gas internal energy is evaluated from the total energy using an inversion scheme implemented in the code assuming γ_{ad} . Proton temperatures, if needed, are computed using the total internal energy u , plasma density ρ and $\gamma_p = 5/3$ ($\Theta_p \equiv (\gamma_p - 1)u/\rho$).

The simulations are two-temperature but to make a connection with the previous studies we use the same GRMHD runs and compute images/light-curves using parametric electron temperature model $R(\beta)$. In this model proton temperatures are calculated from GRMHD quantities and electron temperature is found using formula below:

$$R(\beta) \equiv \frac{T_p}{T_e} = R_{\text{high}} \frac{\beta^2}{1 + \beta^2} + R_{\text{low}} \frac{1}{1 + \beta^2}, \quad (3)$$

where parameter R_{low} and R_{high} are temperature ratios that describe the proton-to-electron temperature ratio in strongly (low plasma β) and weakly (high plasma β) magnetized regions, respectively. To be consistent

with [Event Horizon Telescope Collaboration et al. \(2022, 2024\)](#) we calculate light-curves for $R_{\text{high}} = 1, 10, 40, 160$ and $R_{\text{low}} = 1$. The dimensionless electron temperature that is passed to the synchrotron transfer coefficients in `ipole` is calculated from:

$$\Theta_e = \frac{u m_p}{\rho m_e} \frac{(\gamma_p - 1)(\gamma_e - 1)}{(\gamma_e - 1)R + (\gamma_p - 1)} \quad (4)$$

with internal energy u and rest-mass density ρ provided by GRMHD model. The electron model assumes $\gamma_e = 4/3$ and $\gamma_p = 5/3$, self-consistent with GRMHD simulations in which electrons are relativistic and protons are non-relativistic.

Models with [Kawazura et al. \(2019\)](#) prescription for Q_p^+/Q_e^+ are tagged K and models with parametric electron temperatures are labelled R1-R160 (e.g., model with $R_{\text{low}} = 1$ and $R_{\text{high}} = 160$ is denoted R160). The latter models are referred to as $R(\beta)$ models.

It is reasonable to assume that the energy from the turbulent heating is used to form a non-thermal rather than purely thermal electron distribution function. We consider an exploratory non-thermal model using $\kappa(w, \kappa)$ distribution function ([Xiao 2006](#)) where the distribution parameter

$$w = \frac{(\kappa - 3)}{\kappa} \Theta_e. \quad (5)$$

Here Θ_e is calculated from the electron entropy in exactly same manner as in purely thermal K models (see [Ressler et al. 2015](#)). Equation 5 states that the entire turbulent energy is distributed into κ function. The κ parameter is globally constant. Inspired by the Solar wind studies we assume $\kappa = 4.25$ (e.g., [Livadiotis et al. 2018](#)). In ray-tracing, the radiative transfer coefficients for the κ distribution function are adopted from [Mościbrodzka & Gammie \(2024\)](#). No cutoff is applied to the κ distribution function at high energies because it makes negligible difference when modeling (sub-)millimeter emission.

All radiative transfer simulations are carried out only in regions where $\sigma < \sigma_{\text{cut}} = 1$ (where magnetization parameter $\sigma \equiv 2P_{\text{mag}}/\rho c^2$). This is a standard procedure to avoid modeling emission from near-vacuum jet regions in GRMHD model where proton and electron temperatures are inaccurate (e.g., [Event Horizon Telescope Collaboration et al. 2022](#)).

2.4. Effects of grid resolution

Table 1 lists four test two-temperature MAD a_* = 0 models carried out at different numerical resolutions. Figure 1 shows equatorial cuts through the four models at final integration time, $t_f = 10,000M$. Figure 2 displays the corresponding light-curves for Stokes \mathcal{I} , RM,

LP and CP calculated for time interval between 5,000M and 10,000M at three observing frequencies assuming K model for electron temperatures. In Figure 2 bottom panels display a comparison of M_3 , RM, LP, CP distributions at 229 GHz as a function of grid resolution. There is a very good agreement between M_3 , RM, LP and CP distributions. Although not shown, this is also true for two other neighboring frequencies of 86 and 690 GHz at which the modeled source could be observed.

We conclude that the results presented in the remaining part of this work do not strongly depend on the chosen GRMHD grid resolution. Around the current level of resolutions, which are typically used for building EHT GRMHD model libraries, all modeled quantities are rather settled and the small variations in observables are due to different realizations of turbulence in individual runs¹. We note that we cannot exclude that our models are located at the resolution plateau and that increasing resolution 10 times in each direction may result in the simulation better resolving more physical effects (e.g., better resolution of shocks and reconnection layers may lead to different electron heating in different regions of the flow) that could lead to quantitative and qualitative changes in the emission properties.

3. RESULTS

3.1. Turbulent heating vs. $R(\beta)$ model

Parameters of all the fiducial runs are summarized in Table 1. Figure 3 shows an example of snapshots from our fiducial two-temperature MAD $a_* = 0.9375$ simulation. The fiducial light-curves produced by the GRMHD simulations with different parameters are presented in Appendix A and here we discuss distributions of quantities calculated based on these light-curves.

Figure 4 displays correlations of observables in models R1-160 and K for the default viewing angle $i = 160$ deg, combined for black hole spins $a_* = 0, 0.5, 0.9375$. In M_3 panels, K models are moderately correlated with R1-160 models and typically K models are less variable compared to models R1-160. Spectral slope α_I and CP in model K are highly correlated with those of model R10. This is not the case for RM and for LP for which correlation is much weaker.

Figure 5 shows comparison of distributions of observables for models shown in Figure 4. M_3 , LP and CP averages (and standard deviations) in models K are weakly distinguishable from those in models R1-160.

It is useful to look at properties of maps used to synthesize the integrated observables. Figure 6 shows examples of EHT-like images at 229 GHz produced by a random snapshot of $a_* = 0.5$ simulation with R1,R10,R160 and K electron models for the fiducial viewing angle of $i = 160$ deg. Following [Event Horizon Telescope Collaboration et al. 2024](#) we characterize these images using the following metrics. Net linear and circular polarizations are defined as:

$$m_{\text{net}} \equiv \frac{\sqrt{(\sum_i Q_i)^2 + (\sum_i U_i)^2}}{\sum_i I}, \quad v_{\text{net}} \equiv \frac{\sum_i V_i}{\sum_i I}. \quad (6)$$

The image-averaged linear and circular polarizations defined as:

$$m_{\text{avg}} \equiv \frac{\sum_i \sqrt{Q_i^2 + U_i^2}}{\sum_i I}, \quad v_{\text{avg}} \equiv \frac{\sum_i |V_i|/I_i}{\sum_i I_i}, \quad (7)$$

where sums are carried out over all image pixels. Geometry of linear polarization is described with amplitudes and phases of a complex function

$$\beta_{\text{m}} \equiv \frac{\int_0^\infty \int_0^{2\pi} P(\rho, \phi) e^{-im\phi} \rho d\phi d\rho}{\int_0^\infty \int_0^{2\pi} I(\rho, \phi) \rho d\phi d\rho} \quad (8)$$

where

$$P(\rho, \phi) \equiv Q(\rho, \phi) + iU(\rho, \phi) \quad (9)$$

is the complex polarization vector and where ρ, ϕ are the polar coordinates in the image plane (see [Palumbo et al. 2020](#) or [Event Horizon Telescope Collaboration et al. 2024](#) for details). All these metrics are displayed in the example snapshot in Figure 6. Here it is more evident that the resolved images of models K are most similar to models R10 in both LP and CP. Models R1 differ from K in CP maps. Models R40-160 have already distinct appearance compared to model K, both in LP and CP, as also evident from the comparison of integrated CP. When scored against the existing or a future (total intensity or polarimetric) EHT data, models K may favor similar accretion flow and geometrical parameters as models R10.

It is important to show that the T_p/T_e in K models does not precisely follow the $R(\beta)$ model R10, regardless of Q_p^+/Q_e^+ being strongly dependent on β . Example of T_p/T_e maps for a single snapshot of MAD model with high spin is shown in Figure 7 (top and middle panels). The discrepancy between T_p/T_e in model R10 and K indicates that there is no simple relationship between Q_p^+/Q_e^+ and T_p/T_e as already shown by [Ressler et al. \(2015\)](#) for non-MAD models. Hence, the exact electron temperature consistency is not the main reason behind the similarity of K and R10 models. The difference in T_p/T_e between the models is the smallest close to the

¹ Turbulence is always initialized by a random perturbation of the gas internal energy.

black hole and it increases with radius. The emitting regions close to the black hole have on average $T_p/T_e = 10$. R10 and K models therefore share the scaling \mathcal{M} unit to reproduce the same flux meaning that ρ and B in the synchrotron radiative transfer coefficients are identical leading to similar images. The differences between the model's emissions reflect differences in Θ_e (shown in lower panels in Figure 7) and they seem small from the observational point of view. Due to the Faraday rotation effects LP and RM are the most sensitive among our observables to electron temperatures at small and larger radii. This explains the weaker correlation of LP and RM between R10 and K models visible in Figure 4.

3.2. Importance of other physical effects

3.2.1. Effects of radiative cooling

We carry out radiative GRMHD (GRRMHD) simulation of MAD $a_* = 0$ model to check impact of radiative cooling on electron temperatures and emission properties. The radiative processes included in GRMHD simulation include synchrotron emission, self-absorption, Compton scatterings and bremsstrahlung. To reduce the large computational cost of models with activated multi-frequency radiative transfer the interactions between photon field and gas is allowed only within 100M. Any radiative transfer effects outside of this sphere are negligible. When producing emission the code takes into account the fact that the combined four-momentum of gas and radiation has to be conserved. Emission/absorption/scattering can therefore exert force on gas and change the electron thermodynamics (radiative cooling or heating). In the models considered here, the average optical thickness of gas is $\tau \ll 1$ and luminosities are strongly sub-Eddington, $L \ll L_{\text{Edd}}$, hence it is expected that in models with activated radiative transfer mainly electron thermodynamics is affected and mainly due to synchrotron cooling. Other effects are weak for the considered accretion rates. In Appendix B we present quality factors for the GRRMHD simulation to demonstrate that the interactions between gas and radiation are resolved by adequate number of Monte Carlo samples.

Figure 8 displays volume averaged radial profiles of density, magnetic field, T_p/T_e (or R), and Θ_e in GRMHD and GRRMHD model with K heating mechanism and $\mathcal{M} = 5 \times 10^{11}$ at different time moments, earlier and later in the evolution. All quantities are additionally weighed by ρB factor to show quantities averaged over regions where most of the synchrotron emission comes from. There is a small difference in Θ_e and R radial profiles in models with and without radiative effects, and the difference is due to different realization of

turbulence in each model. Unsurprisingly, at later times in both models $R \sim 10$ for $r < 20M$, consistent with results in Section 3.1. Figure 9 additionally shows that there is no difference in radiative characteristics between GRMHD (K) and GRRMHD (Kcool) models based on 15,000 – 30,000M lightcurves.

Since the test model with cooling has the highest \mathcal{M} among all K models considered in this work, all other K models shown in the paper are expected to cool down even slower than the test case. Radiative cooling effects in MADs with turbulent heating may be neglected when modeling Sgr A* millimeter emission.

3.2.2. Effects of non-thermal electrons

Figure 10 shows comparison of observational characteristics of thermal and non-thermal K fiducial runs. Non-thermal models are slightly less variable compared to the thermal models. Spectral slope α_I , RM, and LP of both thermal and non-thermal models are strongly correlated (the correlation is much stronger in comparison to $R(\beta)$ models). It is evident that the total intensity and linear polarization are not sensitive to details of the distribution function for the considered part of electromagnetic spectrum. CP, on the other hand, is different in both models, hence it may be used to discriminate between distribution functions. We note that CP is usually a more permissive observational constraint compared to LP (see e.g., [Event Horizon Telescope Collaboration et al. 2024](#)). Overall, with exception for CP, all radiative properties of our simple non-thermal models are tightly correlated with their purely thermal counterparts.

3.3. Fiducial models vs. ALMA constraints

Having checked how the results depend on numerical resolution effects and two most relevant physical effects, we can now compare the thermal two-temperature models directly to observations of plasma around Sgr A*.

Figure 11 shows comparison of prograde models K, at various viewing angles, to Sgr A* observables detected by ALMA at 86 and 213-229 GHz in April 2017 ([Wielgus et al. 2022a,b, 2024](#)). The modulation index at both frequencies increases with black hole spin and with inclination angle. In general all models are too variable to match the observed variability (this is also the case for R1-160 models as found in [Event Horizon Telescope Collaboration et al. 2022](#) and shown here in Figure 5) but data strongly favor lower spins at lower inclination angles for which M_3 is the smallest. All models are too optically thin when compared to observations (as is also the case for R1-160 models, compare our Figure 5 with Figure 12, see also [Ricarte et al. 2023](#)). All models also

require external Faraday screen to explain the observations of RM but we notice that models with low viewing angles ($i = 160$ deg, 150 deg) best recover the RM standard deviation towards the source. Linear polarization of $i = 160 - 150$ deg models is consistent with both 229 and 86 GHz measurements. Models with $a_* = 0$ recover CP at 229 GHz, but fail to recover CP at 86 GHz. On the other hand, models with $a_* = 0.9375$ fail to recover CP at 229 GHz, but do recover CP at 86 GHz. Only model with $a_* = 0.5$ does reasonably well with regards to CP at both frequencies. It is possible that a model with black hole spin in-between 0 and 0.5 would be a better fit to ALMA CP data. Among prograde MADs, model with $a_* = 0.5$ is the closest to the ALMA observations altogether.

Although turbulence in the retrograde models reached quasi-stationary state within the emission zone, they are reported separately because they are integrated over shorter times compared to the prograde models. Figure 12 compares statistical properties of light-curves produced by the retrograde MADs. Two-temperature MAD with $a_* = -0.5$ performs better compared to MAD $a_* = -0.9375$ as they are less variable, but worse than MAD $a_* = 0.5$, because prograde models better recover CP at both frequencies.

4. DISCUSSIONS

In this work we have carried out several two-temperature MAD simulations with the main purpose of investigating impact of various numerical parameters on emission properties of these models, in particular grid resolution, but we also investigate impact of physical effects.

Regarding numerical parameters, the two-temperature MAD simulations with turbulent heating of electrons are well converged with respect to the GRMHD grid resolution in agreement with the only published emission convergence test based on non-MAD models (Ressler et al. 2017).

As for physical parameters, radiative cooling can be safely omitted in Sgr A* two-temperature MAD models with turbulent heating, as radiative effects do not significantly affect the electron temperature evolution. These effects may be important when modeling M87, which is a brighter source. We have also carried out first exploratory survey of models in which turbulent heating is dissipated into a non-thermal electron distribution function. Our non-thermal models display very similar characteristics compared to the thermal models. However including physics of non-thermal electrons in the emission models slightly decreases the model variability and alters CP compared to purely thermal models.

Other, also spatially varying, parameters of the κ distribution function could be considered and change our result (e.g., Davelaar et al. 2019).

Long-duration two-temperature simulations indicate that K thermal models are only roughly approximated with R10 models. Using total intensity observables Mizuno et al. (2021) found that the best match to the turbulent heating models are R5 models. Given that their electron temperatures are defined differently (compare their Eq. 8 with our Eq. 4) and are by a factor of ~ 2 smaller than ours, the best match with R10 found here is consistent with the previous finding.

In Section 3.3 we show that none of our long-duration two-temperature K simulations recover general properties of light-curves of Sgr A* observed by ALMA ideally but the ALMA data favor models with lower viewing angles $i = 150 - 160$ deg for which the variabilities of Stokes \mathcal{I} and RM are the smallest. All models have major difficulty with recovering the observed model spectral index, in excellent agreement with previous two-temperature study by Dexter et al. 2020a. All models recover the observed net LP but require introduction of an additional external Faraday screen to recover the observed RM. Only $a_* = 0.5$ model recovers Sgr A* net CP at two observed frequencies, simultaneously, and it is possible that a spin in between 0-0.5 would produce even better fitting results. The preferred moderate/low spin value is consistent with spin estimates based on two-temperature models of Dexter et al. 2020a, although for different than turbulent heating scenario, different initial conditions and different observational datasets. Here we also study evolution of two-temperature MADs for low and high spins for significantly longer time compared to Dexter et al. 2020a.

It is possible that ALMA observes varying compact emission together with less varying extended emission that is not captured in our simulations (C.F. Gammie, private communication) hence it is preferable to compare models with EHT images (or best with the future EHT movies) rather than integrated quantities. When compared to EHT data, K models are expected to favor similar parameter space as R10 models. Polarimetric EHT data of Sgr A* have not yet ruled out all MAD R10 models. In fact 10 out of 20 passing MAD models are R10 models (see Fig. 8 in Event Horizon Telescope Collaboration et al. 2024). Based on similarity between R10 and K appearance, we argue that the turbulent electron heating scenario could be still consistent with the observations of Sgr A*. It is interesting to note that in Event Horizon Telescope Collaboration et al. 2024, MAD models R10 are favored for a set of intermediate viewing angles ($i = 150 - 110$ deg) and positive and

negative spin values. K models could narrow down the range of these two geometrical parameters.

Based on joint total intensity and polarimetric EHT data, the current best-bet MAD model for Sgr A* is R160, not R10 (Event Horizon Telescope Collaboration et al. 2024). We ought to discuss the present results in context of other models for Q_p^+/Q_e^+ . As shown by Dexter et al. (2020a) assuming Howes (2010) turbulent heating model for Q_p^+/Q_e^+ , makes a negligible difference in the MAD electron temperatures compared to Kawazura et al. (2019) model. The reconnection Q_p^+/Q_e^+ model of Rowan et al. 2017, on the other hand, may result in slightly lower (but also around R10) electron temperatures with weaker plasma- β dependency (Mizuno et al. 2021; Dexter et al. 2020a). Lower electron temperatures could make the MAD models optically thicker and less varying (Chan et al. 2024) hence pushing them towards the right direction, but this remains to be thoroughly examined. Weaker dependency on β in models with reconnection heating may result in more disk-like emission of MADs rather than the disk/jet-like emission (Chael et al. 2018) making it more difficult to explain Sgr A* nearly flat radio spectrum (Mościbrodzka & Falcke 2013). Radio spectral slope dependency on Q_p^+/Q_e^+ should be carefully checked with high (jet-resolving) resolutions two-temperature MAD models. Nevertheless, whichever Q_p^+/Q_e^+ scenario above (or a combination of scenarios) is selected, the two-temperature MAD models will have difficulty to naturally develop R160-like electron temperatures near the event horizon. Assuming that MAD is present in Sgr A* system, this may suggest that $R(\beta)$ models are inappropriate for MADs (we further briefly discuss prospects on how to resolve this issue in Appendix C). Alternatively, comparisons of time-varying models to time-averaged EHT images so far (Event Horizon Telescope Collaboration et al. 2022,

2024) introduce a strong bias in the electron temperature parameter inference.

Our simulations are run with constant adiabatic index $\gamma_{\text{ad}} = 13/9$, which is not a self-consistent assumption in regions where electrons are mildly- or sub-relativistic. Recent simulations of Narayan et al. (2022) suggest that MAD dynamics is not affected by the choice of γ_{ad} . It is unclear how different, or varying, γ_{ad} alters the discussed total intensity and polarimetric radiative properties of two-temperature MADs. This topic should be investigated in the future.

Ideal GRMHD models considered here do not include many other, potentially important effects. Additional physics such as resistivity (e.g., Vos et al. 2024), viscosity, plasma composition (Emami et al. 2021; Wong & Gammie 2022), anisotropic pressures (e.g., Foucart et al. 2017) or anisotropic electron distribution functions (e.g., Galishnikova et al. 2023), may all impact the radiative characteristics of MADs. Studying influence of all these effects on observed quantities goes beyond the scope of the current work. The current simulation set constitutes a reference point for future investigations.

- 1 We thank Maciek Wielgus for providing ALMA data
- 2 and comments on the paper. We also thank Andrew
- 3 Chael, Charles Gammie, and Ben Ryan for many of
- 4 their comments. We gratefully acknowledge the HPC
- 5 RIVR consortium (www.hpc-rivr.si) and EuroHPC JU
- 6 (eurohpc-ju.europa.eu) for funding this research by pro-
- 7 viding computing resources of the HPC system Vega at
- 8 the Institute of Information Science (www.izum.si).

Software `ebhlight` (Ryan et al. 2015, 2017, 2018), `ipole` (Mościbrodzka & Gammie 2018), `python` (Oliphant 2007), `matplotlib` (Hunter 2007).

REFERENCES

- Anantua, R., Ressler, S., & Quataert, E. 2020, MNRAS, 493, 1404
- Chael, A., Narayan, R., & Johnson, M. D. 2019, MNRAS, 486, 2873
- Chael, A., Rowan, M., Narayan, R., Johnson, M., & Sironi, L. 2018, MNRAS, 478, 5209
- Chael, A. A., Narayan, R., & Sadowski, A. 2017, MNRAS, 470, 2367
- Chan, C.-K., Psaltis, D., Özel, F., Narayan, R., & Sadowski, A. 2015, ApJ, 799, 1
- Chan, H.-S., Chan, C.-k., Prather, B. S., Wong, G. N., & Gammie, C. 2024, ApJ, 964, 17
- Cruz-Osorio, A., Fromm, C. M., Mizuno, Y., et al. 2022, Nature Astronomy, 6, 103
- Davelaar, J., Mościbrodzka, M., Bronzwaer, T., & Falcke, H. 2018, A&A, 612, A34
- Davelaar, J., Olivares, H., Porth, O., et al. 2019, A&A, 632, A2
- Dexter, J., Jiménez-Rosales, A., Ressler, S. M., et al. 2020a, MNRAS, 494, 4168
- Dexter, J., Tchekhovskoy, A., Jiménez-Rosales, A., et al. 2020b, MNRAS, 497, 4999
- Dihingia, I. K., Mizuno, Y., Fromm, C. M., & Rezzolla, L. 2023, MNRAS, 518, 405

- Dolence, J. C., Gammie, C. F., Mościbrodzka, M., & Leung, P. K. 2009, *ApJS*, 184, 387
- Emami, R., Anantua, R., Chael, A. A., & Loeb, A. 2021, *ApJ*, 923, 272
- Event Horizon Telescope Collaboration, Akiyama, K., Alberdi, A., et al. 2024, *ApJL*, 964, L26
- Event Horizon Telescope Collaboration, Akiyama, K., Alberdi, A., et al. 2022, *ApJL*, 930, L16
- Event Horizon Telescope Collaboration, Akiyama, K., Algaba, J. C., et al. 2021, *ApJL*, 910, L13
- Fishbone, L. G. & Moncrief, V. 1976, *ApJ*, 207, 962
- Foucart, F., Chandra, M., Gammie, C. F., Quataert, E., & Tchekhovskoy, A. 2017, *MNRAS*, 470, 2240
- Fromm, C. M., Cruz-Osorio, A., Mizuno, Y., et al. 2022, *A&A*, 660, A107
- Galishnikova, A., Philippov, A., & Quataert, E. 2023, *ApJ*, 957, 103
- Gammie, C. F., McKinney, J. C., & Tóth, G. 2003, *ApJ*, 589, 444
- Gold, R., McKinney, J. C., Johnson, M. D., & Doeleman, S. S. 2017, *ApJ*, 837, 180
- Howes, G. G. 2010, *MNRAS*, 409, L104
- Hunter, J. D. 2007, *Computing in Science and Engineering*, 9, 90
- Igumenshchev, I. V., Narayan, R., & Abramowicz, M. A. 2003, *ApJ*, 592, 1042
- Jiang, H.-X., Mizuno, Y., Fromm, C. M., & Nathanail, A. 2023, *MNRAS*, 522, 2307
- Kawazura, Y., Barnes, M., & Schekochihin, A. A. 2019, *Proceedings of the National Academy of Science*, 116, 771
- Kim, J. Y., Krichbaum, T. P., Lu, R. S., et al. 2018, *A&A*, 616, A188
- Livadiotis, G., Desai, M. I., & Wilson, L. B., I. 2018, *ApJ*, 853, 142
- McKinney, J. C., Tchekhovskoy, A., & Blandford, R. D. 2012, *MNRAS*, 423, 3083
- Mizuno, Y., Fromm, C. M., Younsi, Z., et al. 2021, *MNRAS*, 506, 741
- Mościbrodzka, M. & Falcke, H. 2013, *A&A*, 559, L3
- Mościbrodzka, M., Falcke, H., & Shiokawa, H. 2016, *A&A*, 586, A38
- Mościbrodzka, M., Falcke, H., Shiokawa, H., & Gammie, C. F. 2014, *A&A*, 570, A7
- Mościbrodzka, M. & Gammie, C. F. 2018, *MNRAS*, 475, 43
- Mościbrodzka, M. & Gammie, C. F. 2024, *ApJ*, 968, 6
- Mościbrodzka, M., Gammie, C. F., Dolence, J. C., & Shiokawa, H. 2011, *ApJ*, 735, 9
- Narayan, R., Chael, A., Chatterjee, K., Ricarte, A., & Curd, B. 2022, *MNRAS*, 511, 3795
- Narayan, R., Igumenshchev, I. V., & Abramowicz, M. A. 2003, *PASJ*, 55, L69
- Oliphant, T. E. 2007, *Computing in Science and Engineering*, 9, 10
- Palumbo, D. C. M., Wong, G. N., & Prather, B. S. 2020, *ApJ*, 894, 156
- Petersen, E. & Gammie, C. 2020, *MNRAS*, 494, 5923
- Porth, O., Mizuno, Y., Younsi, Z., & Fromm, C. M. 2021, *MNRAS*, 502, 2023
- Proga, D. & Begelman, M. C. 2003, *ApJ*, 592, 767
- Ressler, S. M., Tchekhovskoy, A., Quataert, E., Chandra, M., & Gammie, C. F. 2015, *MNRAS*, 454, 1848
- Ressler, S. M., Tchekhovskoy, A., Quataert, E., & Gammie, C. F. 2017, *MNRAS*, 467, 3604
- Ricarte, A., Gammie, C., Narayan, R., & Prather, B. S. 2023, *MNRAS*, 519, 4203
- Rowan, M. E., Sironi, L., & Narayan, R. 2017, *ApJ*, 850, 29
- Ryan, B. R., Dolence, J. C., & Gammie, C. F. 2015, *ApJ*, 807, 31
- Ryan, B. R., Ressler, S. M., Dolence, J. C., Gammie, C., & Quataert, E. 2018, *ApJ*, 864, 126
- Ryan, B. R., Ressler, S. M., Dolence, J. C., et al. 2017, *ApJL*, 844, L24
- Sadowski, A., Wielgus, M., Narayan, R., et al. 2017, *MNRAS*, 466, 705
- Scepi, N., Dexter, J., & Begelman, M. C. 2022, *MNRAS*, 511, 3536
- Tchekhovskoy, A., Narayan, R., & McKinney, J. C. 2011, *MNRAS*, 418, L79
- Vos, J. T., Olivares, H., Cerutti, B., & Mościbrodzka, M. 2024, *MNRAS*, 531, 1554
- Walker, R. C., Hardee, P. E., Davies, F. B., Ly, C., & Junor, W. 2018, *ApJ*, 855, 128
- Wielgus, M., Issaoun, S., Martí-Vidal, I., et al. 2024, *A&A*, 682, A97
- Wielgus, M., Marchili, N., Martí-Vidal, I., et al. 2022a, *ApJL*, 930, L19
- Wielgus, M., Moscibrodzka, M., Vos, J., et al. 2022b, *A&A*, 665, L6
- Wong, G. N. & Gammie, C. F. 2022, *ApJ*, 937, 60
- Xiao, F. 2006, *Plasma Physics and Controlled Fusion*, 48, 203
- Yfantis, A. I., Mościbrodzka, M. A., Wielgus, M., Vos, J. T., & Jimenez-Rosales, A. 2024, *A&A*, 685, A142
- Zhao, S.-S., Huang, L., Lu, R.-S., & Shen, Z. 2023, *MNRAS*, 519, 340

a_*	ID	R_{low}	R_{high}	$i[^\circ]$	$\frac{\dot{M}}{10^{17}}$	$\langle \dot{M} \rangle [M_\odot/\text{yr}]$	$t_s[\text{M}]$	$t_f[\text{M}]$	$\Delta t[\text{M}]$	resolution	cooling
Convergence study models											
0	K_HHR	-	-	160	5	1.0×10^{-8}	5,000	10,000	10	360x120x192	no
0	K_HR	-	-	160	5	1.1×10^{-8}	5,000	10,000	10	240x240x128	no
0	K_MR	-	-	160	5	1.0×10^{-8}	5,000	10,000	10	240x120x128	no
0	K_LR	-	-	160	5	1.2×10^{-8}	5,000	10,000	10	120x120x128	no
Fiducial models											
-0.9375	K	-	-	160	2	4.6×10^{-9}	10,000	14,000	10	266x120x128	no
-0.9375	K	-	-	150	2	4.6×10^{-9}	10,000	14,000	10	266x120x128	no
-0.9375	K	-	-	130	2	4.6×10^{-9}	10,000	14,000	10	266x120x128	no
-0.9375	K	-	-	110	2	4.6×10^{-9}	10,000	14,000	10	266x120x128	no
-0.5	K	-	-	160	5	6.9×10^{-9}	10,000	14,000	10	240x120x128	no
-0.5	K	-	-	150	4.5	6.2×10^{-9}	10,000	14,000	10	240x120x128	no
-0.5	K	-	-	130	4	5.5×10^{-9}	10,000	14,000	10	240x120x128	no
-0.5	K	-	-	110	4	5.5×10^{-9}	10,000	14,000	10	240x120x128	no
0	R1	1	1	160	3	4.2×10^{-9}	15,000	30,000	10	240x120x128	no
0	R10	1	10	160	5	7×10^{-9}	15,000	30,000	10	240x120x128	no
0	R40	1	40	160	7	9.8×10^{-9}	15,000	30,000	10	240x120x128	no
0	R160	1	160	160	10	1.4×10^{-8}	15,000	30,000	10	240x120x128	no
0	K	-	-	160	5	7×10^{-9}	15,000	30,000	10	240x120x128	no
0	K	-	-	150	5	7×10^{-9}	15,000	30,000	10	240x120x128	no
0	K	-	-	130	4	5.6×10^{-9}	15,000	30,000	10	240x120x128	no
0	K	-	-	110	4	5.6×10^{-9}	15,000	30,000	10	240x120x128	no
0.5	R1-160	1	1	160	2	2.7×10^{-9}	15,000	30,000	10	240x120x128	no
0.5	R10	1	10	160	3	4.1×10^{-9}	15,000	30,000	10	240x120x128	no
0.5	R40	1	40	160	5	6.9×10^{-9}	15,000	30,000	10	240x120x128	no
0.5	R160	1	160	160	8	1.1×10^{-8}	15,000	30,000	10	240x120x128	no
0.5	K	-	-	160	3	4.1×10^{-9}	15,000	30,000	10	240x120x128	no
0.5	K	-	-	150	3	4.1×10^{-9}	15,000	30,000	10	240x120x128	no
0.5	K	-	-	130	3	4.1×10^{-9}	15,000	30,000	10	240x120x128	no
0.5	K	-	-	110	3	4.1×10^{-9}	15,000	30,000	10	240x120x128	no
0.9375	R1	1	1	160	1.5	2.0×10^{-9}	15,000	30,000	10	266x120x128	no
0.9375	R10	1	10	160	2	2.7×10^{-9}	15,000	30,000	10	266x120x128	no
0.9375	R40	1	40	160	4	5.5×10^{-9}	15,000	30,000	10	266x120x128	no
0.9375	R160	1	160	160	6	8.3×10^{-9}	15,000	30,000	10	266x120x128	no
0.9375	K	-	-	160	2	2.7×10^{-9}	15,000	30,000	10	266x120x128	no
0.9375	K	-	-	150	2	2.7×10^{-9}	15,000	30,000	10	266x120x128	no
0.9375	K	-	-	130	2	2.7×10^{-9}	15,000	30,000	10	266x120x128	no
0.9375	K	-	-	110	2	2.7×10^{-9}	15,000	30,000	10	266x120x128	no
Exploratory models											
0	K,cooling	-	-	-	5	8×10^{-9}	15,000	30,000	10	240x120x128	yes
0.5	K,non-thermal	-	-	160	3	4.1×10^{-9}	15,000	30,000	10	240x120x128	no
0.5	K,non-thermal	-	-	150	3	4.1×10^{-9}	15,000	30,000	10	240x120x128	no
0.5	K,non-thermal	-	-	130	3	4.1×10^{-9}	15,000	30,000	10	240x120x128	no
0.5	K,non-thermal	-	-	110	3	4.1×10^{-9}	15,000	30,000	10	240x120x128	no

Table 1. List of GRMHD/GRRMHD and radiative transfer models resulting in different time-series of images. Accretion rates \dot{M} are time-averages between t_s and t_f .

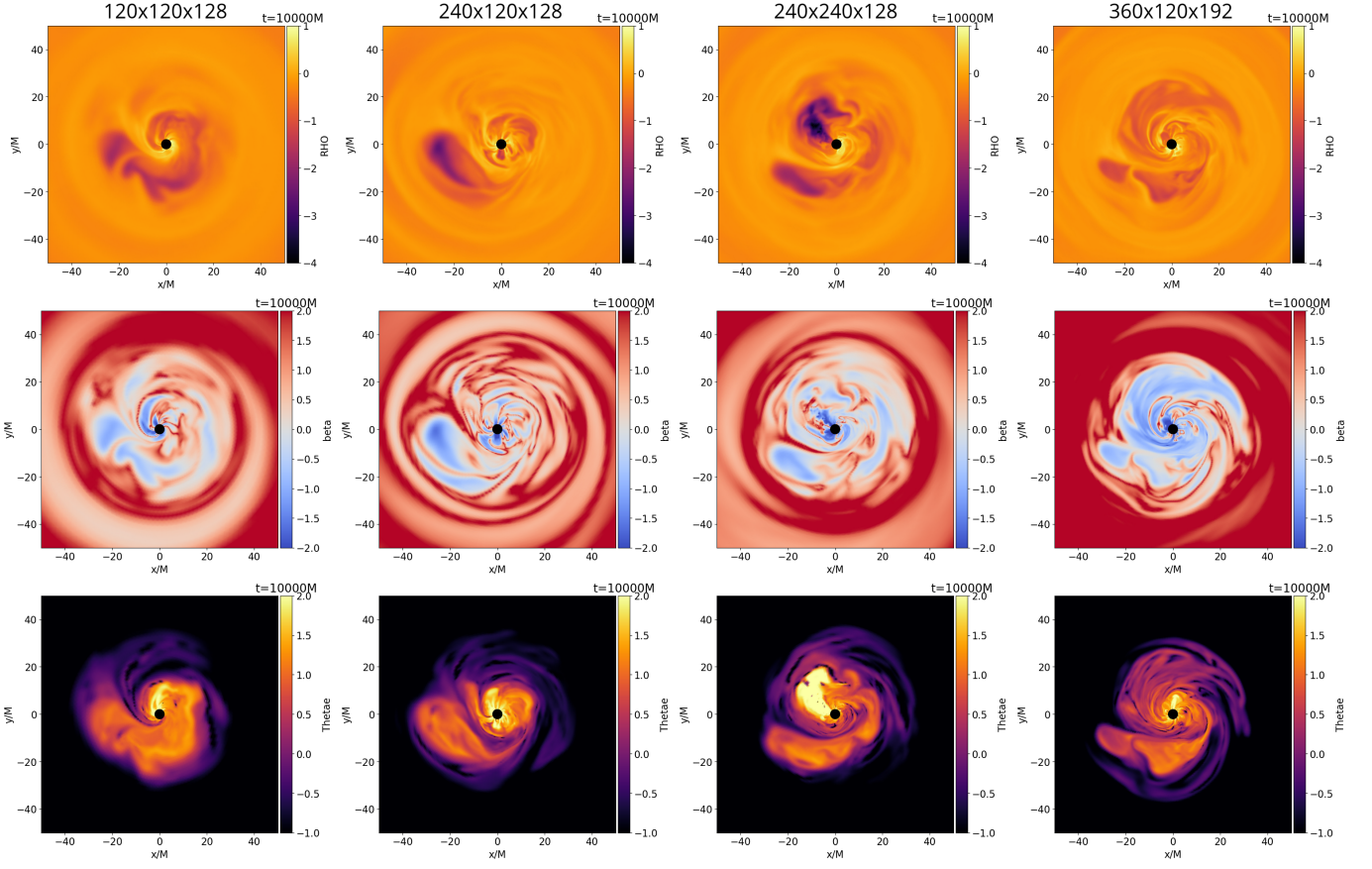


Figure 1. Equatorial density (top panels), plasma β (middle panels), and K model electron temperature (bottom panels) maps in various resolution two-temperature MAD $a_* = 0$ models at $t = 10,000M$.

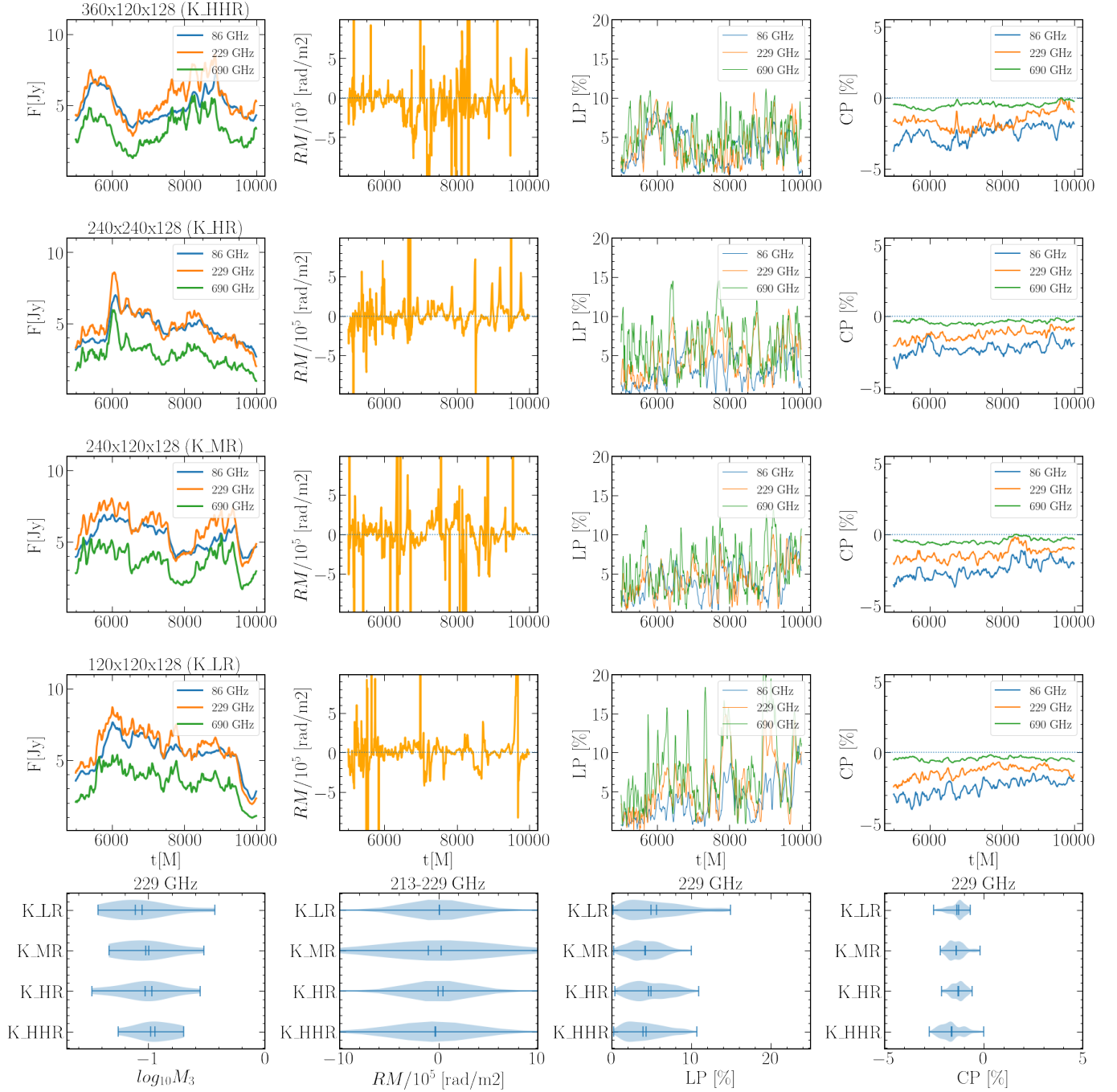


Figure 2. Comparison of Stokes I , RM, LP, and CP in two-temperature MAD $a_* = 0$ models with increasing grid resolution (Table 1). The vertical bars in the violin plots mark mean, median and upper/lower limits of the distribution.

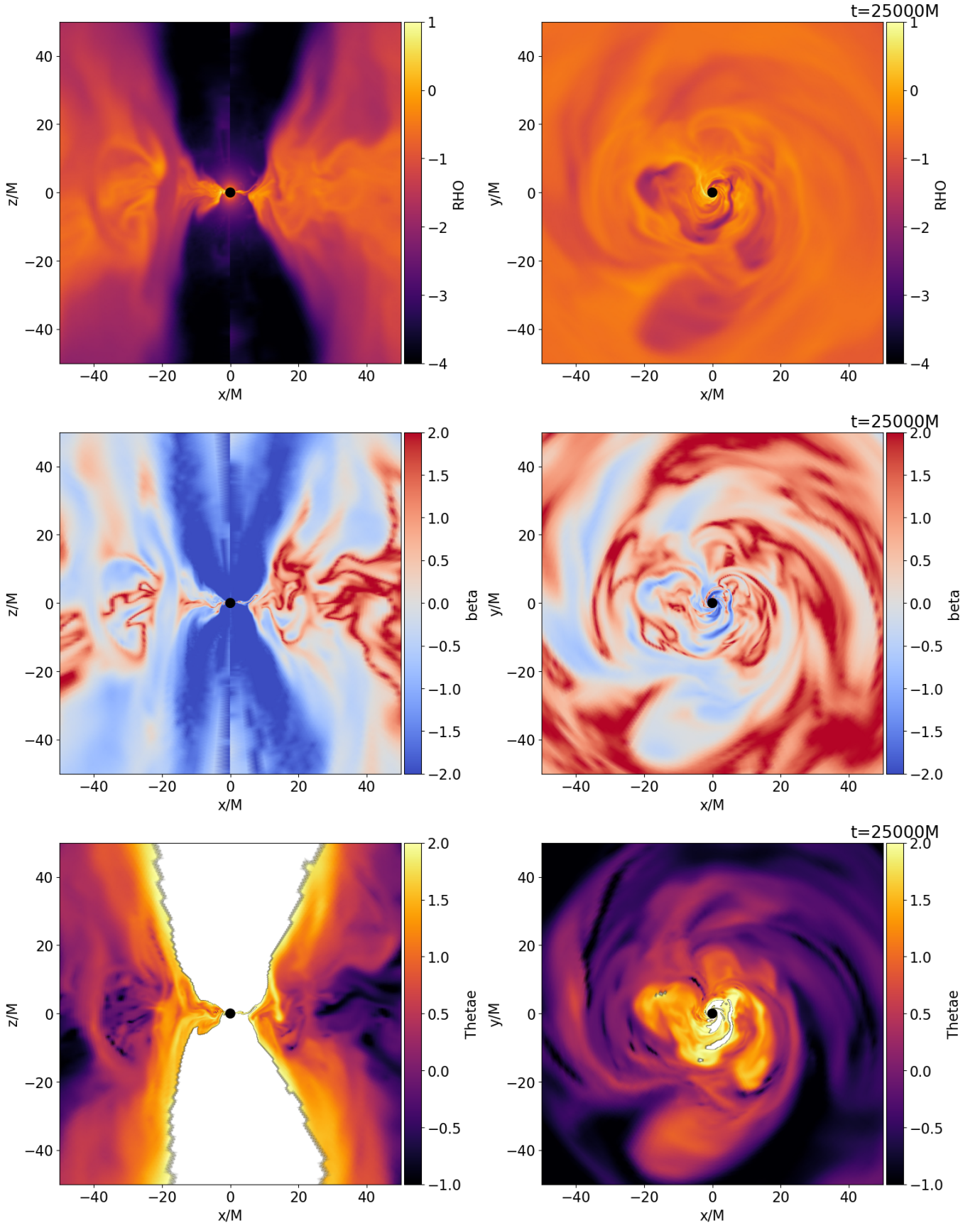


Figure 3. Examples of meridional and equatorial slices showing plasma density (top panels), plasma β parameter (middle panels) and K model electron temperatures (bottom panels) in fiducial MAD $a_* = 0.9375$ simulation at $t = 25,000M$ (see Table 1). The panel with electron temperature masks uncertain region not taken into account in radiative transfer calculations.

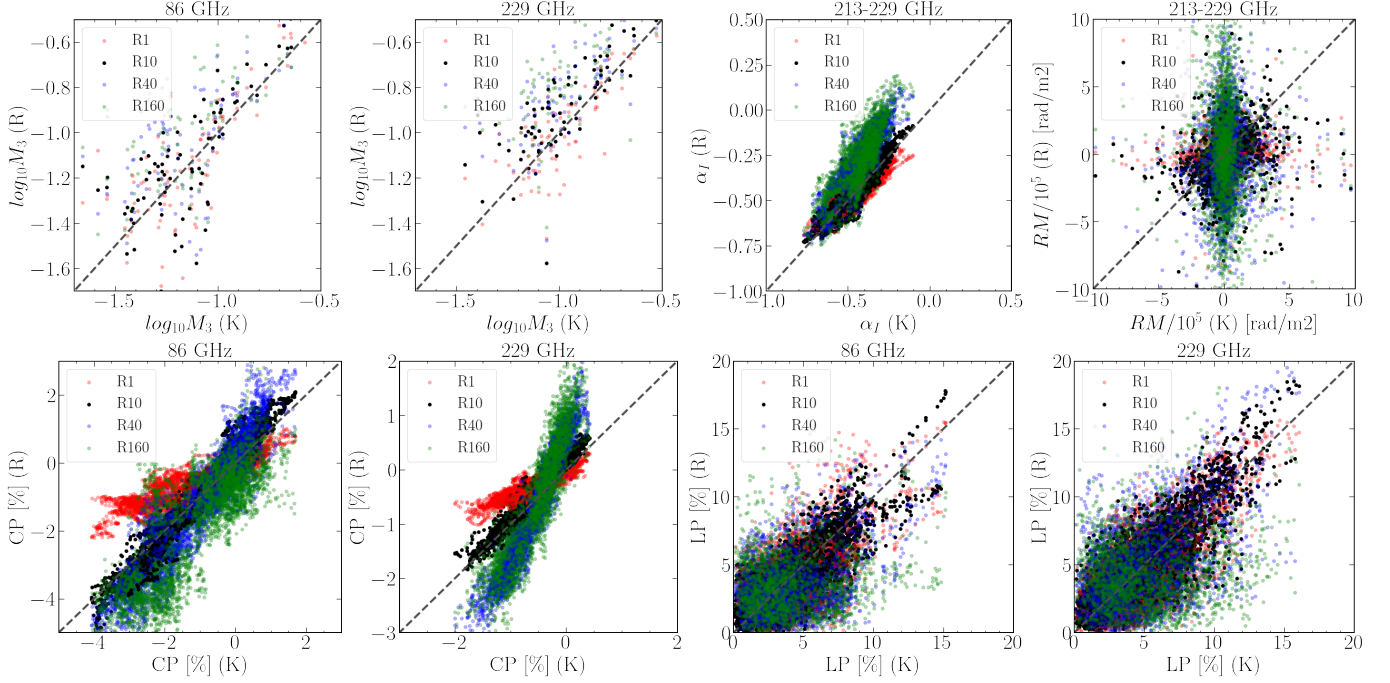


Figure 4. Comparison of the net radiative properties for MAD K and R1-160 (spins $a_* = 0, 0.5, 0.9375$ combined) models calculated for the default viewing angle $i = 160$ deg. Top panels show modulation indices of Stokes \mathcal{I} light-curves at 86 and 229 GHz; spectral slopes and rotation measure distributions around 229 GHz. In the bottom panels we show distribution of fractional circular (CP) and linear (LP) polarizations for 86 and 229 GHz. All net quantities are build based on light-curves from 15,000-30,000M.

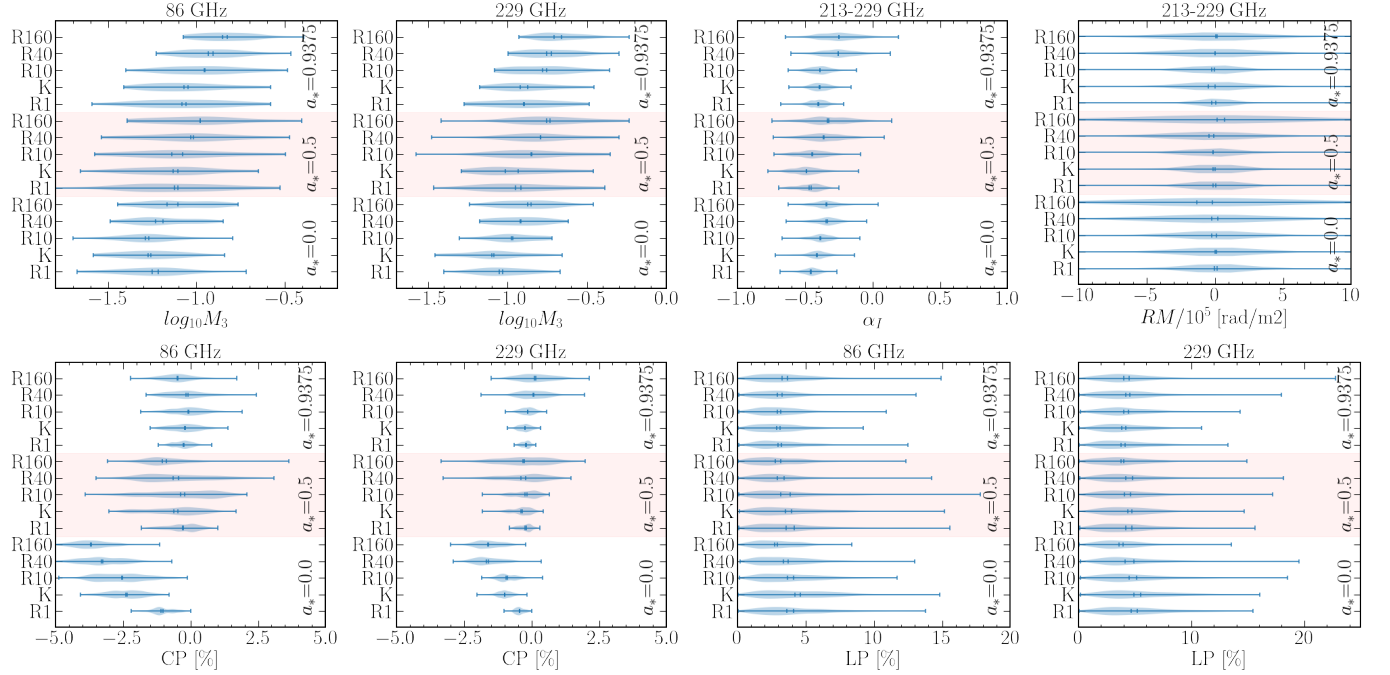


Figure 5. Comparison of distributions of various observables in MAD models K and R1-160 observed at $i = 160$ deg. The light red background is introduced to visually separate models with different spins ($a_* = 0, 0.5, 0.9375$).

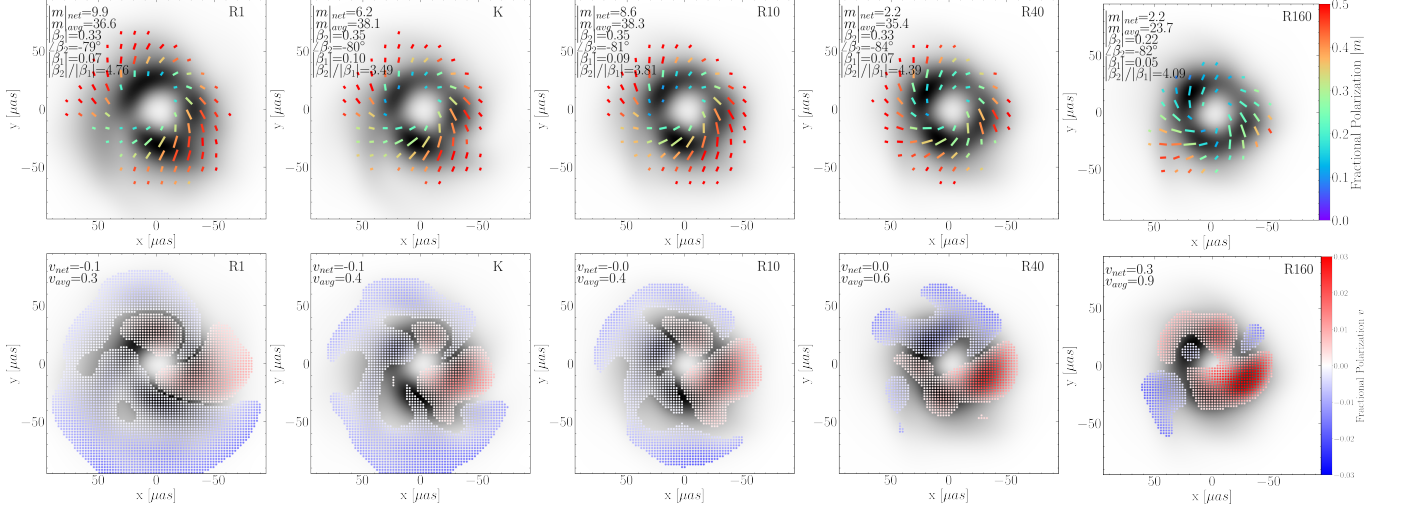


Figure 6. Comparison of snapshot images of MAD $a_* = 0.5$ models K,R1,R10,R40 and R160 at frequency of 229 GHz for the fiducial viewing angle $i = 160$ deg. Images are blurred by a Gaussian kernel with FWHM= $20\mu\text{as}$ to imitate resolution of EHT. In the top panels the gray scale is used for total intensity and color ticks illustrate the linear polarization of the emission. Linearly polarized fraction of total intensity is marked with color and tick length is proportional to $P \equiv \sqrt{Q^2 + U^2}$. We do not show linear polarization in regions where flux in P drops below 20% of its maximum. In the bottom panels the fractional circular polarization is plotted as points. We do not show circular polarization in regions where $|V|$ drops below 5% of its maximum. K models are close to R10 models but details of polarimetric characteristics are slightly different.

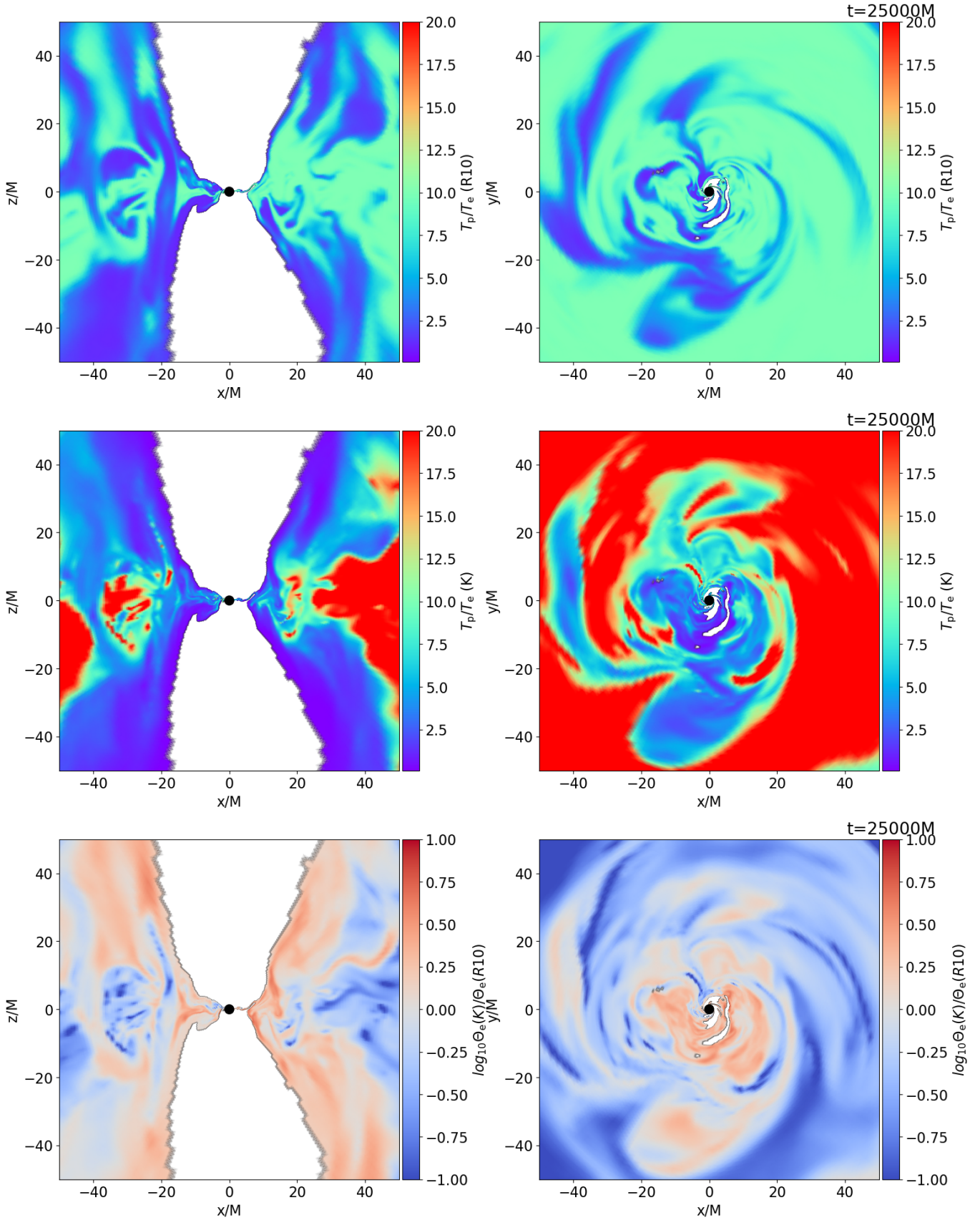


Figure 7. Examples of meridional and equatorial slices showing T_p/T_e (top panels show T_p/T_e in model R10 and middle panels show T_p/T_e in model K) and ratio of K and R10 Θ_e (bottom panels) in MAD $a_* = 0.9375$ at $t = 25,000M$. The uncertain regions, not taken into account in radiative transfer calculations, are masked.

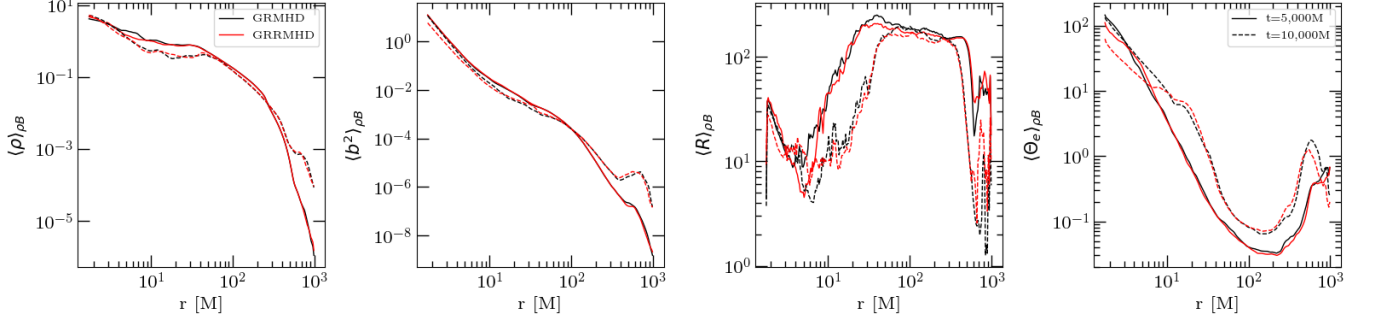


Figure 8. Comparison of radial profiles of density, magnetic field strength (square), proton-to-electron temperature ratio (R) and electron temperatures in GRMHD (black lines) and GRRMHD (red lines) models. All quantities are dimensionless or in code units and they are all angle averaged, where averaging of a quantity Q is defined as $\langle Q(r, t) \rangle \equiv \int_0^{2\pi} \int_0^\pi Q(r, \theta, \phi, t) \sqrt{-g} d\theta d\phi / \int_0^{2\pi} \int_0^\pi \sqrt{-g} d\theta d\phi$ where g is the metric determinant. All quantities are also weighted with ρB factor to show quantities averaged over regions where most of the synchrotron emission comes from. Different line styles correspond to different time moments of the MAD evolution.

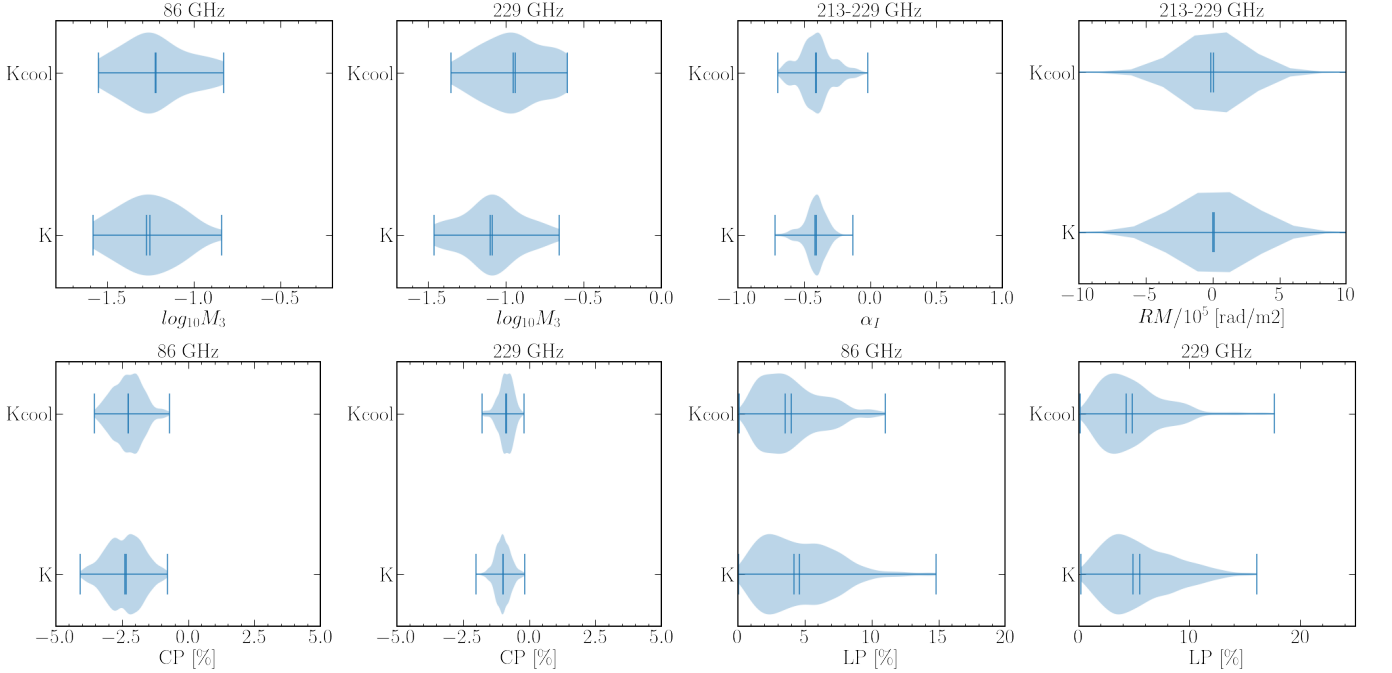


Figure 9. Comparison of radiative characteristics of GRMHD (K) and GRRMHD (Kcool) models with $a_* = 0$ spin computed for lightcurves in time interval 15,000 – 30,000M.

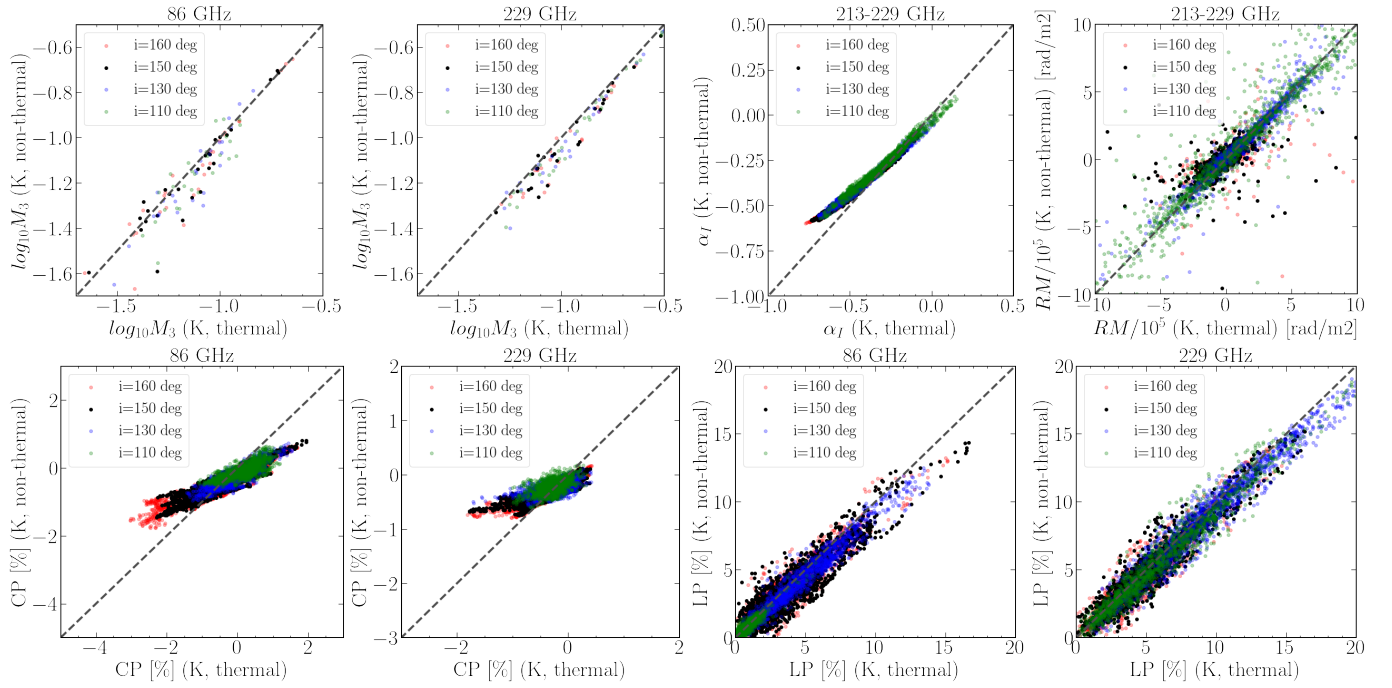


Figure 10. Comparison of radiative characteristics of thermal and non-thermal MAD models with $a_* = 0.5$. All panels are same as in Figure 4 but colors indicate models with different viewing angles rather than different R_{high} parameters.

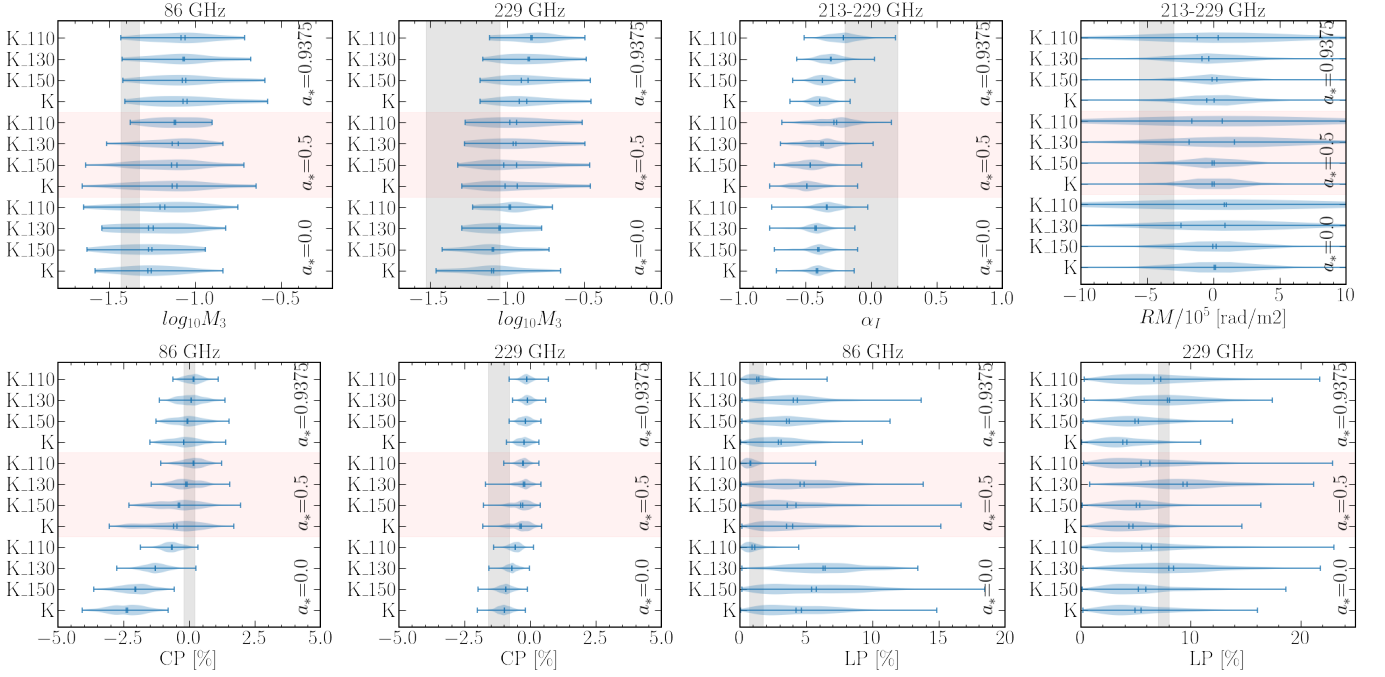


Figure 11. Comparison of radiative characteristics of MAD models K ($a_* = 0, 0.5, 0.9375$) at a default viewing angle of $i = 160$ deg (K) and three additional angles $i = 150, 130, 110$ deg (K_150, K_130, K_110) to observations of Sgr A* collected by ALMA in April 2017 (86 GHz data collected on April 3rd and 230 GHz data collected on April 6-11) and presented in [Wielgus et al. \(2022a,b, 2024\)](#) (gray bands). The light red background is introduced to visually separate models with different spins.

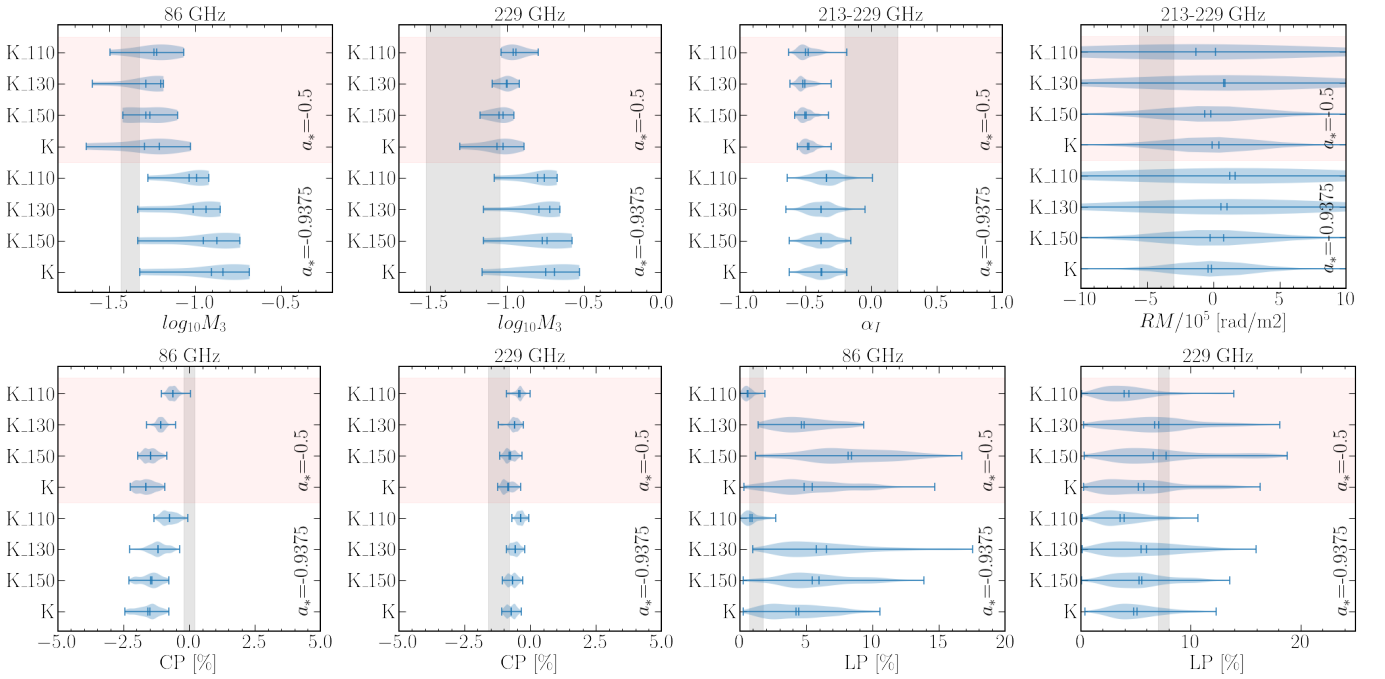


Figure 12. Same as Figure 11 but for retrograde models K.

APPENDIX

A. LIGHT CURVES

The main text of this manuscript presents statistical properties of light-curves from MAD simulations with different spin values. Figures 13 through 15 present light-curves of individual zero and prograde models for the default viewing angle $i = 160$ deg. Here in addition to 86 and 229 GHz we also show light-curves at 690 GHz for visual comparison.

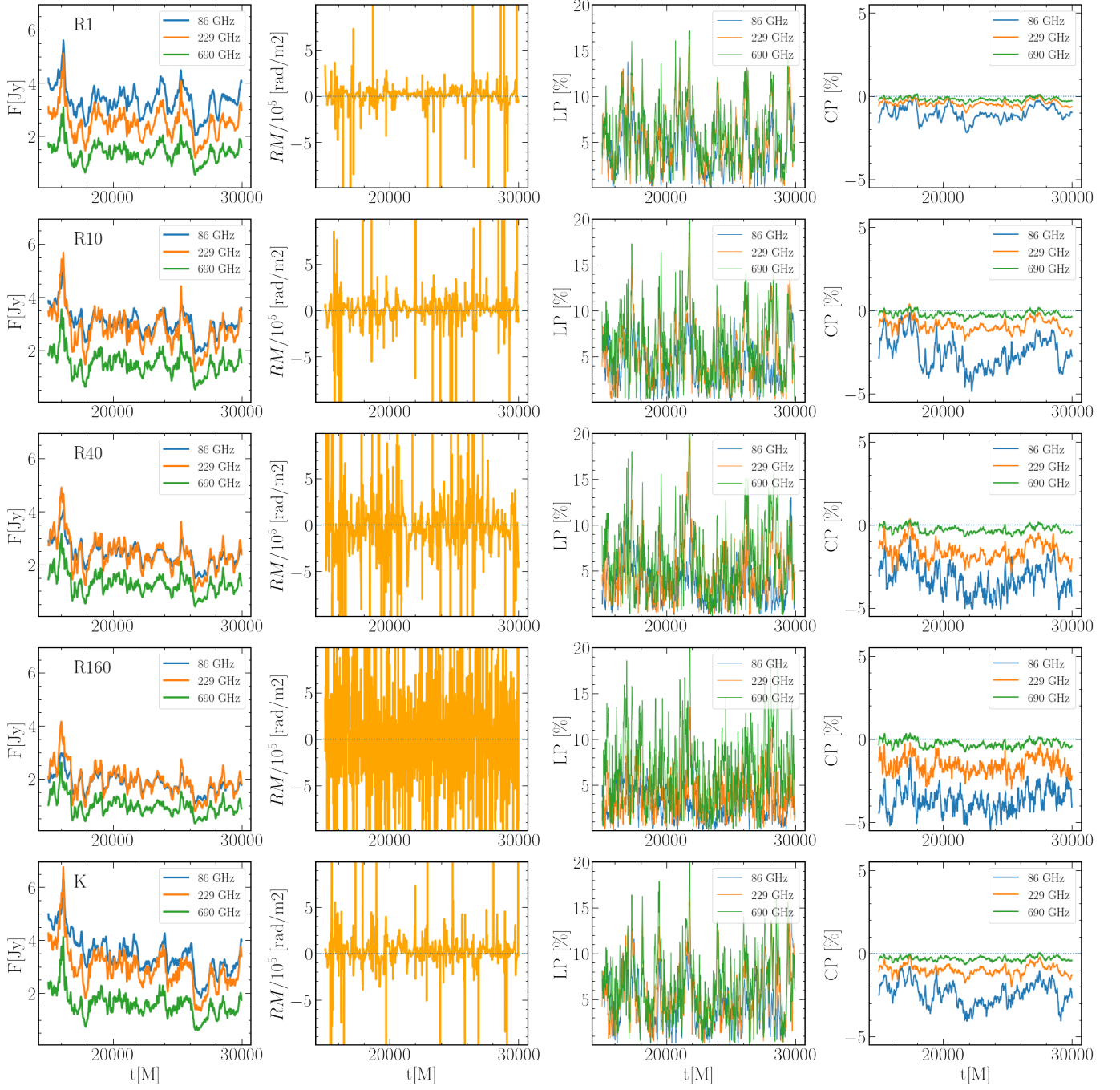


Figure 13. Radiative signatures for MAD $a_* = 0$ model at the default viewing angle of $i = 160$ deg. Panels from left to right display Stokes \mathcal{I} (86, 229, 690 GHz), RM (213-229 GHz), LP (86, 229, 690 GHz) and CP (86, 229, 690 GHz). Panels from top to bottom show models R1-160, and K.

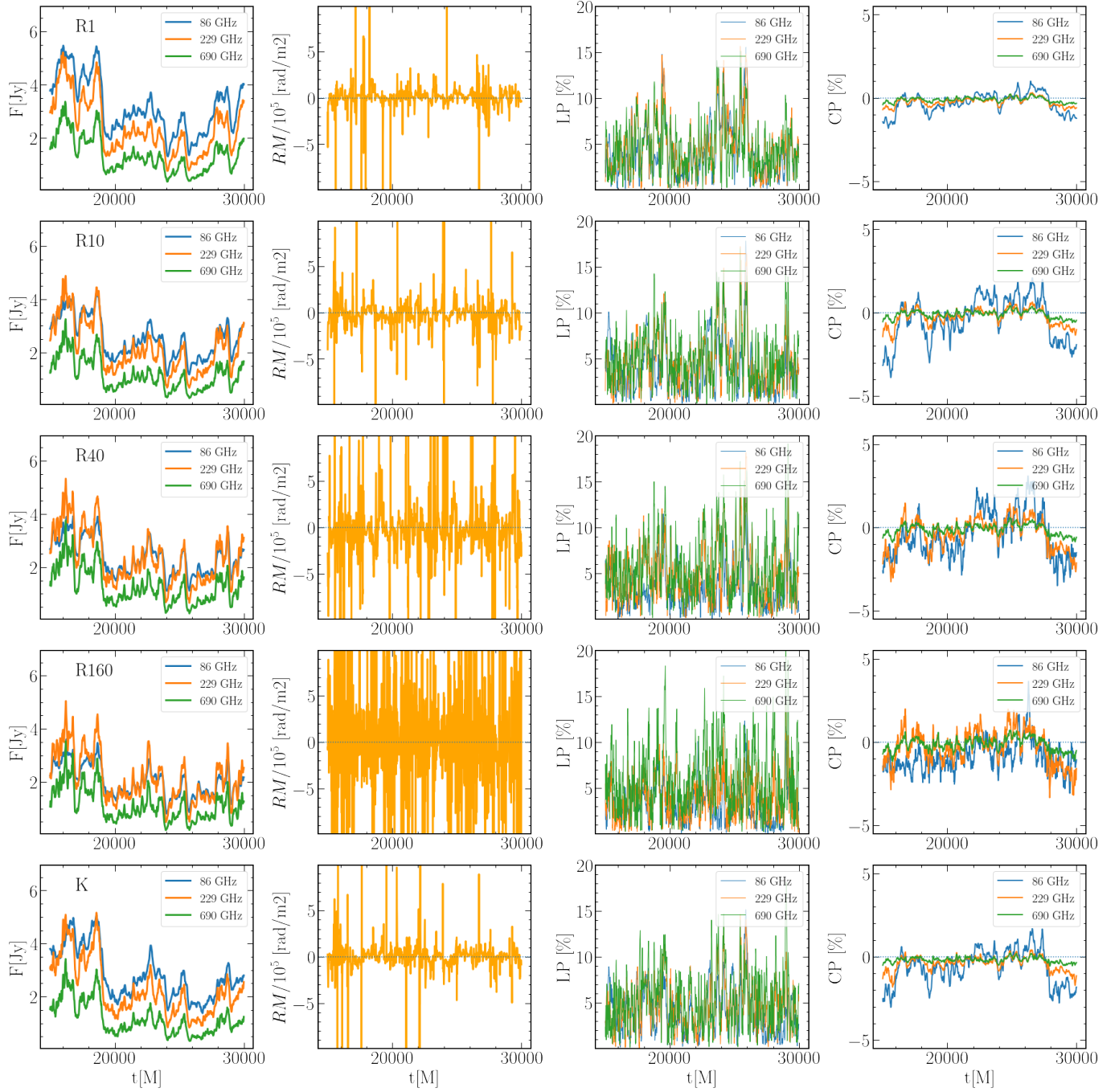


Figure 14. Same as in Figure 13 but for MAD $a_* = 0.5$ models R1-160 and K.



Figure 15. Same as in Figure 13 but for MAD $a_* = 0.94$ models R1-160 and K.

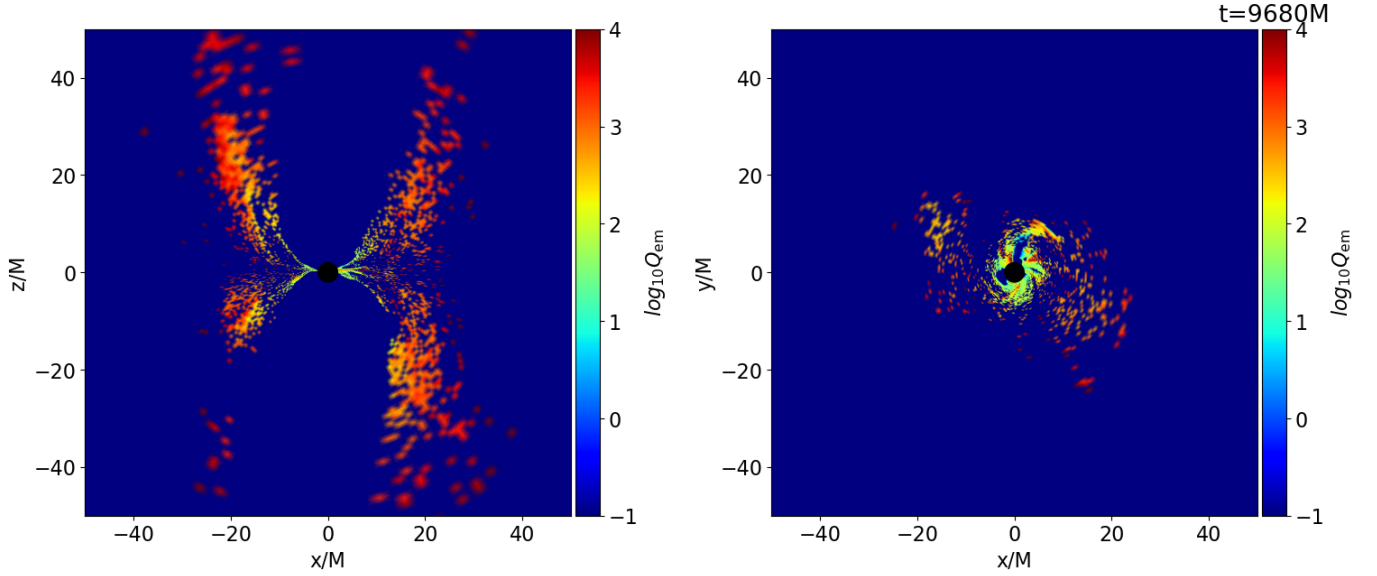


Figure 16. Meridional and equatorial slices showing number of superphotons emitted within one synchrotron cooling timescale in GRRMHD MAD $a_* = 0$ model. The figure illustrates not only the quality of the GRRMHD model but also the origin of the synchrotron emission in the two-temperature MAD models.

B. GRRMHD

In `ebhlight` the multifrequency radiative transport is carried out using Monte Carlo scheme in which the radiation field is simulated with a large number of superphoton particles representing even larger number of physical photons (see code description in [Ryan et al. \(2015\)](#) for exact definitions). To make sure that the radiative cooling of plasma is well captured, for each fluid element the Monte Carlo scheme has to produce a sufficient number of photon particles within the electron cooling timescale.

The electron cooling timescale (in M units) writes:

$$\tau_{\text{cool}} = \frac{u_{e,\text{code}}}{\Lambda_{\text{code}}} \quad (\text{B1})$$

where $u_{e,\text{code}}$ is the electron internal energy provided by the two-temperature model (in the code units) and where Λ_{code} is the synchrotron cooling rate (also in the code units). In c.g.s units the cooling rate reads (Eq. A4 from [Mościbrodzka et al. 2011](#)):

$$\Lambda_{\text{c.g.s.}} = \frac{16B^2 e^4 n_e \Theta_e^2}{3c^3 m_e^2}. \quad (\text{B2})$$

where conversion to code units is: $\Lambda_{\text{code}} = \Lambda_{\text{cgs}} \mathcal{L}^3 / \mathcal{M}$. Figure 16 shows GRRMHD quality factor Q_{em} , a number of superphotons emitted within τ_{cool} , for a snapshot of GRRMHD around $t=10,000M$. $Q_{\text{em}} \gg 10$ in the inner disk ($r < 10M$) and along the jet wall, indicating reasonable sampling in regions where the radiative cooling is the most efficient.

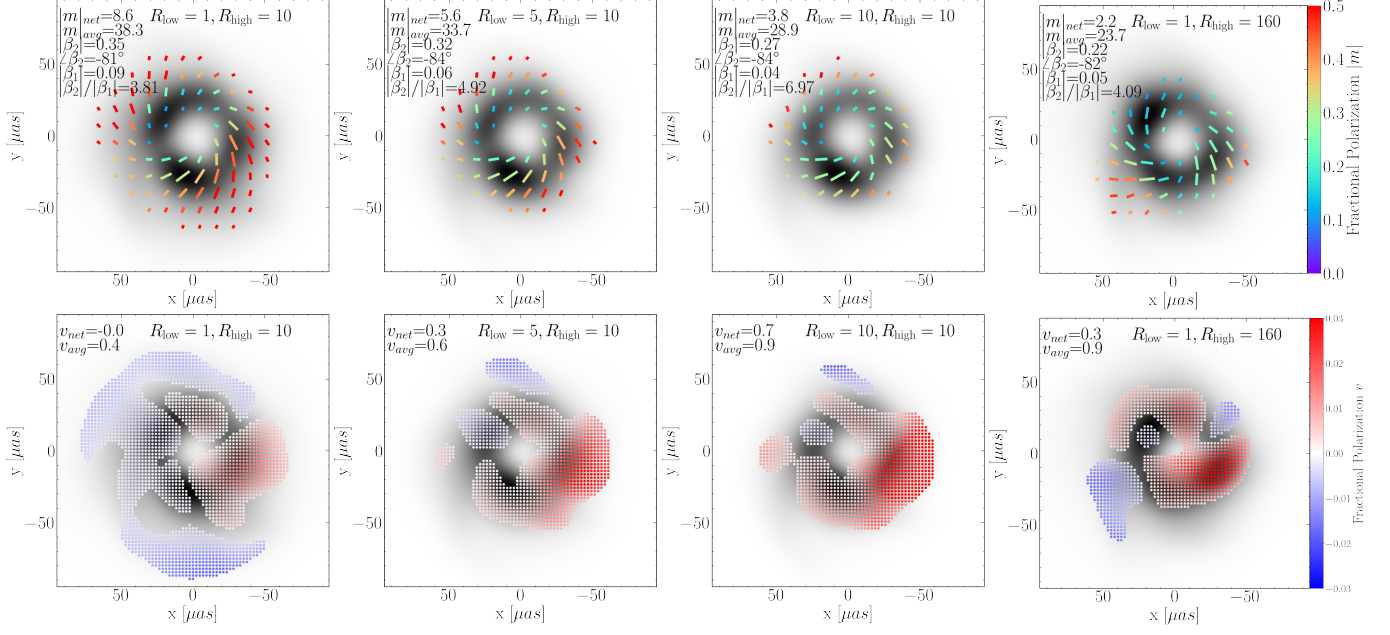


Figure 17. Polarimetric images of a single GRMHD MAD $\alpha_* = 0.5$ snapshot. Panels show the same quantities as in Figure 6 but only for $R(\beta)$ models with different assumptions of R_{low} parameter in Equation 3. All models are normalized with different \mathcal{M} to reproduce the same total flux. From left to right: $\mathcal{M}/10^{17} = 3, 4, 5, 8$.

C. THE ISSUE OF R_{LOW} PARAMETER IN $R(\beta)$ MODEL AND PARAMETER INFERENCE

When estimating electron temperature parameters using polarimetric images of Sgr A*, [Event Horizon Telescope Collaboration et al. \(2024\)](#) assumed that in Equation 3, $R_{\text{low}} = 1$. What happens if we relax the assumption about R_{low} ? Figure 17 shows the impact of varying R_{low} parameter on the linear and circular polarimetric images of Sgr A*. Images of the MAD with $(R_{\text{low}}, R_{\text{high}}) = (10, 10)$ start to resemble those with $(R_{\text{low}}, R_{\text{high}}) = (1, 160)$. It is therefore possible that polarimetric scoring of models with $R_{\text{low}} \sim 10$ could lead to different best-fit values of $R_{\text{high}} \ll 160$. If this is indeed the case, which has to be carefully verified in the future, electron temperature parameter estimations using $R(\beta)$ models with $R_{\text{low}} \sim 10$ have a better chance to converge with some of the discussed $Q_{\text{p}}^+/Q_{\text{e}}^+$ models, proving that particle-in-cell models applied to GRMHD simulations correctly predict the order of magnitude of electron heating in the collisionless plasma.